High extinction ratio, low insertion loss, optical switch based on an electrowetting prism

Mo Zohrabi,[1,*] **Wei Yang Lim,**[2] **Victor M. Bright,**[2] **and Juliet T. Gopinath**[1,3]

[1]*Department of Electrical, Computer, and Energy Engineering, University of Colorado, Boulder, Colorado 80309, United States*
[2]*Department of Mechanical Engineering, University of Colorado, Boulder, Colorado 80309, United States*
[3]*Department of Physics, University of Colorado, Boulder, Colorado 80309, United States*
[*]*mo.zohrabi@colorado.edu*

Abstract: An optical switch based on an electrowetting prism coupled to a multimode fiber has demonstrated a large extinction ratio with speeds up to 300 Hz. Electrowetting prisms provide a transmissive, low power, and compact alternative to conventional free-space optical switches, with no moving parts. The electrowetting prism performs beam steering of $\pm 3°$ with an extinction ratio of 47 dB between the ON and OFF state and has been experimentally demonstrated at scanning frequencies of 100–300 Hz. The optical design is modeled in Zemax to account for secondary rays created at each surface interface (without scattering). Simulations predict 50 dB of extinction, in good agreement with experiment.

1. Introduction

High extinction ratio, fast optical switches are critical in many applications such as atomic clocks [1, 2], optical and quantum communications [3], fiber-optic switches [4], and displays [5]. The optical switch actuation can be mechanical or nonmechanical. The majority of mechanical-based optical switches use piezoelectric transducers [6, 7] or solenoid actuators [8], but can be prone to failure. Nonmechanical optical shutters and switches often use acousto-optic [9] or electro-optic devices. MEMS-based optical switches with optical, electrical, and mechanical functionalities have been integrated in optical telecommunication networks with a large number of interconnects [10, 11]. Recently, a wide variety of liquid-based optical devices have been demonstrated as adaptive optical elements, including electrowetting lenses and prisms [12–19], liquid crystals [20, 21], pressure driven elastic membranes [22], and other optofluidic devices [23–27]. In this work, we have implemented an electrowetting prism to demonstrate a high extinction ratio, low insertion loss, fast, nonmechanical optical switch.

The electrowetting principle [28–34] enables us to manipulate a liquid's contact angle on solid surfaces with applying an external electric field. More recently, electrowetting-on-dielectric (EWOD) devices have been developed with an addition of an insulating layer and a hydrophobic layer [28, 34]. The advancements on EWOD device fabrication [12, 35–41] and various studies on liquid combinations [12, 41–45] have resulted in a wide variety of EWOD-based optical devices, such as lenses and microlenses [12–14], prisms and microprism arrays [17–19], multielectrode devices [46], and electrowetting displays [47–50]. The electrowetting-based devices are appealing due to their transmissive nature, compact size with minimal voltage requirements, and lack of moving parts. Recently, other nonmechanical electrowetting actuation mechanisms were employed to investigate optical switches/shutters such as tunable irises [51–55] and optical switches/shutters based on opaque ink, oil droplet actuation, and total internal reflection [56–64]. Ultrasmooth liquid-liquid interfaces are ideal for optical switch applications with a high rejection rate and low scattering loss [65–67]. Previously, an optical switch based on total internal reflection with an EWOD lens was demonstrated with an extinction ratio of 66 dB and an overall response

time of ~4.9 seconds [60]. Here, we demonstrate a simple transmissive optical design that uses an EWOD prism to scan a focused beam across a multimode fiber with scanning frequency of up to 300 Hz, with an extinction ratio of ~47 dB and an insertion loss of 1 dB. Lastly, we have performed non-sequential ray tracing analysis to trace partially reflected and refracted rays and simulate the experimental results.

2. Electrowetting principle and fabrication

Electrowetting is a technique to change liquid's wetting properties by an external electric field [28–33]. Modern electrowetting devices incorporate an electrode, a dielectric, and a hydrophobic layer. The dielectric layer insulates the conductive fluid from the actuating electrode(s), preventing any electrochemical reactions [28–34]. The hydrophobic layer lowers contact angle hysteresis while enhancing the initial contact angle [68–71]. This is a more robust actuation mechanism known as electrowetting-on-dielectric (EWOD). The contact angle modulation is described by the Lippmann-Young equation [30, 33], $\cos\theta = \cos\theta_\circ + (\epsilon\epsilon_\circ/2\gamma d)V^2$, where θ is the contact angle after actuation with the applied voltage V, $\theta_\circ$ is the initial contact angle at $V = 0$ V, ϵ and d are the effective permittivity of the dielectric layers and its thickness, and γ is the surface tension of the liquid-liquid interface. EWOD devices are often assembled in a cylindrical glass tube filled with a polar and nonpolar liquids, and by applying a voltage through the dielectric layer the curvature of the liquid-liquid interface is altered. EWOD lenses use a uniform electrode coated around the cylindrical glass tube and are implemented in optical applications that benefit from tunable variable focal length, such as cameras [12, 72] and microscopy [73–75]. Two or more electrode EWOD devices, functioning as an EWOD prism, have been implemented in beam steering [16–18] applications like two-photon scanning microscopy [76] and light detection and ranging (LiDAR) [77]. By increasing the number of electrodes to 8 or 16, we can generate a custom shape liquid-liquid interface that can be used for both on- and off-axis optical aberration correction [46, 78, 79]. In addition to individual EWOD devices, an array of lenses and prisms has been studied extensively [13, 14, 16, 19].

The EWOD prism is constructed in a cylindrical glass tube based on our previous work [41, 76, 77] as depicted in Fig. 1. The cylindrical glass tube has an inner diameter of 4 mm, outer diameter of 6 mm, and a height of 5 mm. Transparent Indium Tin Oxide (ITO) electrodes are deposited on the sidewalls of the glass tube using a direct current sputtering process. The EWOD prism consists of two separated electrodes on the sidewalls of the glass tube patterned using a 3D printing assisted shadow masking technique. The electrode patterning and deposition step is
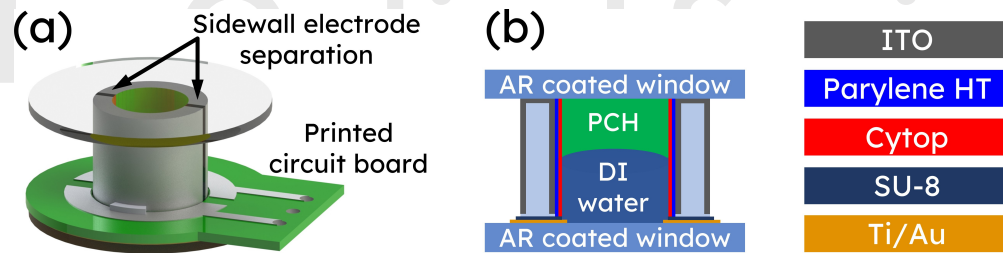

Fig. 1. (a) A perspective view of the two-electrode prism device, labeled with electrode gap separation and printed circuit board assembly. (b) Schematic of the two-electrode prism device. The device is constructed in a cylindrical glass tube with Indium Tin Oxide (ITO) sidewall electrodes, Parylene HT as the dielectric and Cytop as the hydrophobic layer. An anti-reflection (AR) coated optical window patterned with an annular pattern of Ti/Au/Ti serves as the ground electrode. The device is filled with deionized (DI) water and 1-Phenyl-1-cyclohexene (PCH). The device is capped with an AR coated optical window.

followed by coating the inner sidewalls of the glass tube with a ~3.7 μm Parylene HT layer using a vapor phase deposition process (Specialty Coating Systems). The device is then dip coated in a 10% Cytop solution (CTL-809M in CTSOLVE-100E, AGC Chemical Company). The glass tube with thus functionalized sidewalls is epoxy bonded to a 12.7 mm diameter anti-reflection (AR) coated glass window with annular Titanium/Gold (Ti/Au, 20 nm/ 300 nm) electrode patterned on it. The Ti/Au annulus has an inner diameter of 3.75 mm and acts as the ground electrode for the device. The device is sequentially filled with ~31.5 μL of deionized (DI) water and 1-phenyl-1-cyclohexene (PCH), followed by placing the AR coated optical window on top of the device [see Fig. 1(b)]. The ratio of gravitational to surface tension forces is characterized by the Bond number, $B_\circ = \rho g R^2/\gamma$. In our case, the two liquids are density matched, with a Bond number $<< 1$, resulting in an optical device that is insensitive to gravitational distortions. The EWOD device is actuated by applying a sinusoidal AC voltage, with a carrier frequency of 3 kHz and no offset voltage. The reliability and performance of an electrowetting device can be strongly affected by the dielectric layer properties and the characteristics of the liquids. Typically, a pinhole free material with high dielectric constant and a high breakdown strength is deposited as a thin layer. Many studies have been carried out on improving the reliability of EWOD devices based on the choice of single- and multi-layer dielectrics [80–83]. The choice of liquid combinations is critical in developing a reliable electrowetting device. One of the main challenges is to increase the refractive index difference between the two liquids while maintaining density match condition and having a low freezing point, low viscosity, and low turbidity after thermal shock [42]. The dielectric thickness (Parylene HT ~3.7 μm and Cytop ~500 nm) are chosen based on our previous work [41], so as to provide contact angle tuning range from 173° at 0 V to 60° at 170 V_{rms}. In this work, we numerically simulate the liquid-liquid interface of a two-electrode EWOD device used in the experiment and implement it into an optical design to demonstrate a high-extinction ratio optical switch using non-sequential ray tracing.

3. Optical setup and simulation

The optical setup (shown in Fig. 2) used to test the switch is composed of a single two-electrode EWOD device (prism) followed by an achromatic doublet lens (effective focal length of 4.4 mm)
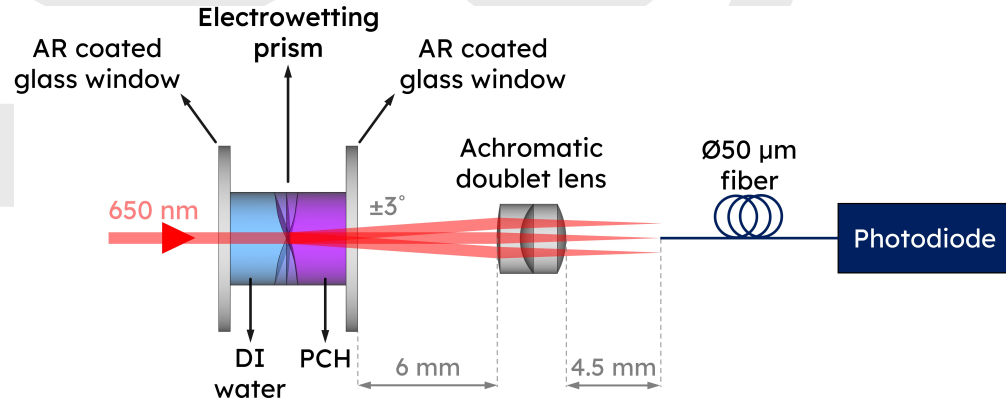

Fig. 2. Schematic optical design of the electrowetting prism optical switch modeled in Zemax for a collimated input beam diameter of 1.2 mm ($1/e^2$), λ = 650 nm. The switch consists of a tunable pressure-driven lens (Optotune EL10-30 – not shown here), an electrowetting prism, an achromatic doublet lens (effective focal length of 4.4 mm), and a multimode fiber with a core diameter of 50 μm. The fiber is coupled to a photodiode. The EWOD prism produced a ±3° scanning beam. Three configurations are shown here with steering angles of 0° and ±3°.

and a multimode fiber with a core diameter of 50 μm. A tunable pressure-driven lens (Optotune EL10-30) is positioned 140 mm from the EWOD prism to adjust the focusing condition while coupling to the multimode fiber. The schematic of the setup, modeled in Zemax OpticStudio [84] (ray tracing software), is shown in Fig. 2 without the tunable pressure driven lens. To simulate the optical setup, we have modeled the curvature of the meniscus between the two liquids by using Young-Laplace equation [69–71, 85–90], which describes the equilibrium shape of the liquid-liquid interface. The general Young-Laplace equation with contact condition is given by, $\nabla u(x,y)/(1 + |\nabla u(x,y)|^2)^{1/2}) = \cos\gamma$, where $u(x,y)$ is the equilibrium surface profile and γ is the contact angle at the glass sidewall boundary. The steady-state contact angles of the DI water and PCH combination were experimentally determined to be 173° with no applied voltage and 60° at 170 V_{rms} [41]. The contact angle variation is used as the boundary condition in the Young-Laplace equation. We have used Matlab's partial differential equation (PDE) toolbox to solve the Young-Laplace equation and the results are compared to computational fluid dynamics simulation based on two-phase Laminar flow in COMSOL Multiphysics [78, 91–95]. The simulated liquid-liquid interface is imported into Zemax OpticStudio to perform ray tracing.

Figure 2 depicts the modeled setup in Zemax OpticStudio sequential mode with the 3 configurations that represent the simulated liquid-liquid interface for steering angles of 0° and ±3°. The distances between all the optical elements are kept fixed (similar to the experimental conditions), while the focal length of the tunable pressure-driven lens is optimized for minimum
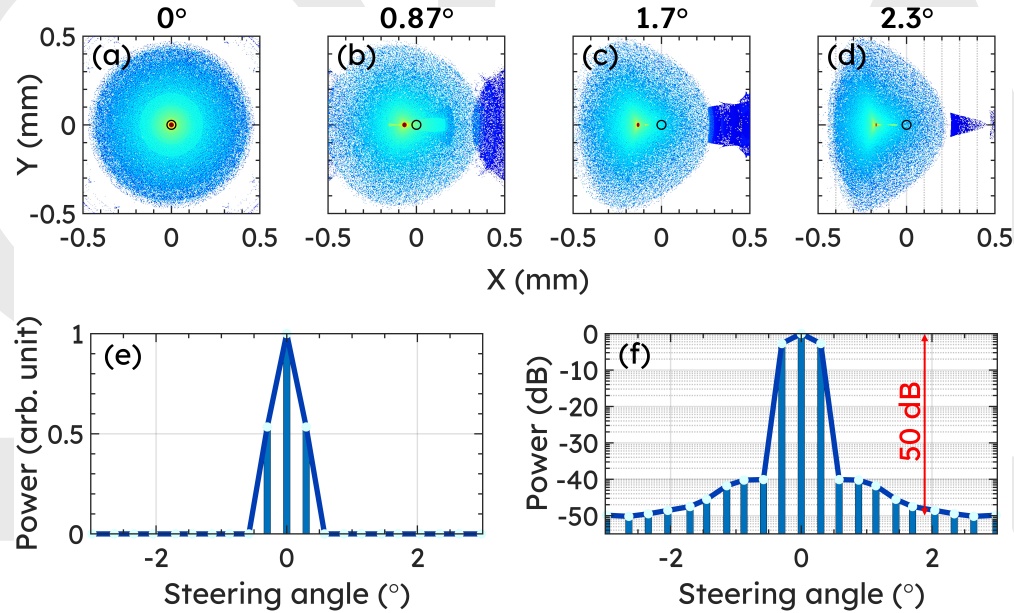

Fig. 3. (a)–(d) The incoherent irradiance maps (incoherent ray intensity distribution for various incident angles) at the imaging plane of the optical setup (Fiber entrance plane in Fig. 2) for steering angles of 0°, 0.87°, 1.7°, and 2.3°. The dark circle at (0,0) with 50 μm diameter represents the fiber core position in the imaging plane. The imaging plane shows the point-spread function for different steering angles. The scattered ray pattern in the imaging plane is a result of secondary rays split at each optical interface. (e)–(f) The integrated power within the 25 μm radius as a function of steering angles of ±3° plotted in linear and log scale. The extinction ratio defined as: $10\log(P_{max}/P_{min})$, where P_{max} and P_{min} are the power transmitted in the ON and OFF states, respectively. Optical switching with a high extinction ratio of 50 dB is obtained by steering the beam to angles larger than ±2.5°.

spot size in the imaging plane. A similar procedure has been implemented in the experiments. Next, the optical design is converted from sequential to non-sequential mode in Zemax. Non-sequential ray tracing is a powerful tool for tracing rays in a system with multiple optical paths in which certain types of analysis such as stray and scattered light are practical [84]. Twenty-one liquid-liquid interfaces are simulated in Matlab and imported to Zemax corresponding to a steering of ±3°. A total of one million rays were traced to fill a 0.5 mm diameter detector plane with pixel size of 2 μm. An incoherent irradiance map (incoherent ray intensity distribution for various incident angles) is generated in the detector plane for various steering angles. Examples of these irradiance maps for steering angles of 0°, 0.87°, 1.7°, and 2.3° are shown in Fig. 3(a)–3(d). The dark circle at (0,0) with 50 μm diameter represents the fiber core in these figures.

In non-sequential ray tracing, a ray that strikes a surface can either reflect, refract, total internal reflect (TIR), scatter, split, diffract, or get absorbed (or a combination of these) depending on the properties of the surface. Effects such as ray splitting divide each reflected beam into a large number of secondary rays that dominate the detector plane and appear as scattered pattern in Fig. 3(a)–3(d). Figure 3(a) shows the point-spread function without any steering (on-axis configuration). The shape of the point spread function is altered at larger steering angles (> 1°) as the optical aberrations such as coma take effect when a beam travels through a tilted slightly curved liquid-liquid surface [see Fig. 3(d)]. In general, optical switches are characterized by the extinction ratio, defined as: $10\log(P_{max}/P_{min})$, where P_{max} and P_{min} are the power transmitted between the ON and OFF states, respectively. To evaluate the extinction ratio, the irradiance map for each steering angle is integrated within the 25 μm radius. The normalized power is plotted in linear and log scale, respectively, as shown in Fig. 3(e)-3(f). At the ON state the beam is aligned to the multimode fiber (at 0° - on the optical axis), with high transmission, while steering the beam to angles larger than ±2.5° diminished the transmission through the fiber corresponding to OFF state. This results in optical switching with an extinction ratio of 50 dB by steering the beam between the ON and OFF states (or steering the beam to angles larger than ±2.5°).

4.   Experimental results and discussions

We used a continuous-wave 650 nm diode laser, with a collimated beam diameter of 1.2 mm ($1/e^2$), to characterize the extinction ratio of the EWOD prism as a function of steering angle. In addition, we have investigated the scanning frequency of the proposed optical switch. The experimental setup resemble the optical design sketched in Fig. 2. The apparatus is composed of a two-electrode, 4-mm inner diameter EWOD prism followed by an achromatic doublet lens (effective focal length of 4.4 mm) and a multimode 50 μm core fiber patch coupled into a Si-biased detector (Thorlabs DET36A). A tunable pressure-driven lens (Optotune EL10-30) is placed 140 mm behind the EWOD prism to adjust the focusing condition while coupling to the fiber. The power transmitted through the design is measured by collecting the light onto Si-biased detector which is connected to a lock-in amplifier (SRS SR830). We have coupled a laser power of 0.1 mW through the system with coupling efficiency of 80%. To actuate the EWOD prism, we have generated two sinusoidal voltages at 3 kHz with zero voltage offset using a high-speed analog output device (NI PCIe 6738) and amplified them with an 8-channel high-voltage amplifier (OKO Bipolar HV amplifier).

The initial contact angle of the liquid-liquid interface is 173° with no applied voltages. The contact angle can be tuned to 60° by applying 170 V [41]. Actuating the two electrodes symmetrically generates a curvature change similar to an EWOD lens device. We apply a voltage difference between the two electrodes to perform beam steering in the EWOD prism that will generate a tilt across the liquid-liquid interface as shown in Fig. 2. The collimated beam is first coupled to the multimode fiber. The EWOD prism is added to the optical path and actuated symmetrically by applying 72 V$_{rms}$ to both electrodes. The fiber coupling is optimized by adjusting the alignment of the EWOD prism and fine-tuning the pressure driven lens. To achieve
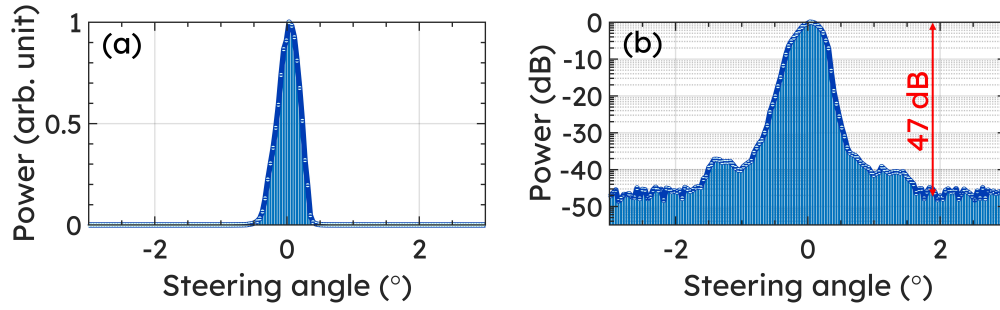
Fig. 4. (a)–(b) Transmitted power through the optical switch as a function of steering angle of the EWOD prism in linear and log scale, respectively. The extinction ratio defined as: $10\log(P_{max}/P_{min})$, where P_{max} and P_{min} are the power transmitted in the ON and OFF states. The transmitted beam exhibits ~47 dB of extinction ratio by steering the beam to angles > 2°. The standard deviation errors are evaluated from 20 measurements. The standard deviation error bars are smaller than the data points (circle marker).

beam steering, the EWOD prism is driven at the bias voltage of 72 V_{rms} with a voltage difference of ± 10 V applied out of phase between the two electrodes, resulting in one-dimensional beam scanning corresponding to steering angles of ± 3°. The scanning frequency was chosen to be 0.2 Hz due to the long time constant setting of the lock-in amplifier (a large time constant > 100 ms is mandatory to improve the signal to noise ratio (SNR) of the system and it also greatly increases the response time of the lock-in amplifier).

The optical performance of the optical switch is characterized in terms of extinction ratio in the ON and OFF states, and the scanning frequency. The power transmitted through the optical switch as a function of steering angle is shown in Fig. 4 in linear and log scales, respectively. We measure an extinction ratio of ~47 dB for the beam that is transmitted through the device (ON state) versus the beam steered to angles > ± 2° (OFF state). To ensure measurement reliability, the results presented here were repeated 20 times. The standard deviation errors are evaluated from 20 measurements and added to the data points in Fig 4(a) and 4(b). The standard deviation error bars are smaller than the data points (circle marker). The results show that the extinction ratio was maintained at 47 dB without altering the driving voltages of the electrowetting prism in the 20 measurements. The measured extinction ratio of 47 dB is comparable, but slightly smaller than the 50 dB predicted by simulation results. This is mainly due to lack of scattering in the optical simulation. The effect of optical scattering from the EWOD prism can be discarded due to the ultrasmooth surface of the liquid-liquid interface (in the sub-nanometer range) [65–67]. The other surfaces make a large contribution to optical scattering, such as the AR coated windows mounted on the top and bottom of the device and the coupling lens. Modeling the scattering from these surfaces in conjunction with non-sequential ray tracing is rather complex and beyond the scope of our work. The scattering from these surfaces reduces the extinction rate in the simulation which is consistent with observed experimental results. The extinction ratio limitation is mainly due to the secondary (stray) rays that circulate within the optical setup.

To perform dynamic beam scanning, the electrodes are driven with two amplitude modulated sinusoidal voltage functions, π out of phase, with a set sweeping frequency. The sweeping frequencies ranged from 100–300 Hz, well below the carrier wave frequency (3 kHz). The electrowetting prism is initially biased by applying 72 V (3 kHz) to both electrodes. The liquid-liquid interface is stable in this state and the voltage differential is defined as: (V_{left} − V_{right}), applied symmetrically around the voltage of 72 V with various sweeping frequencies. Due to the faster scan frequency, the transmission through the multimode fiber is collected on a photodiode by a data acquisition card (MC USB201) for various sweeping frequencies.
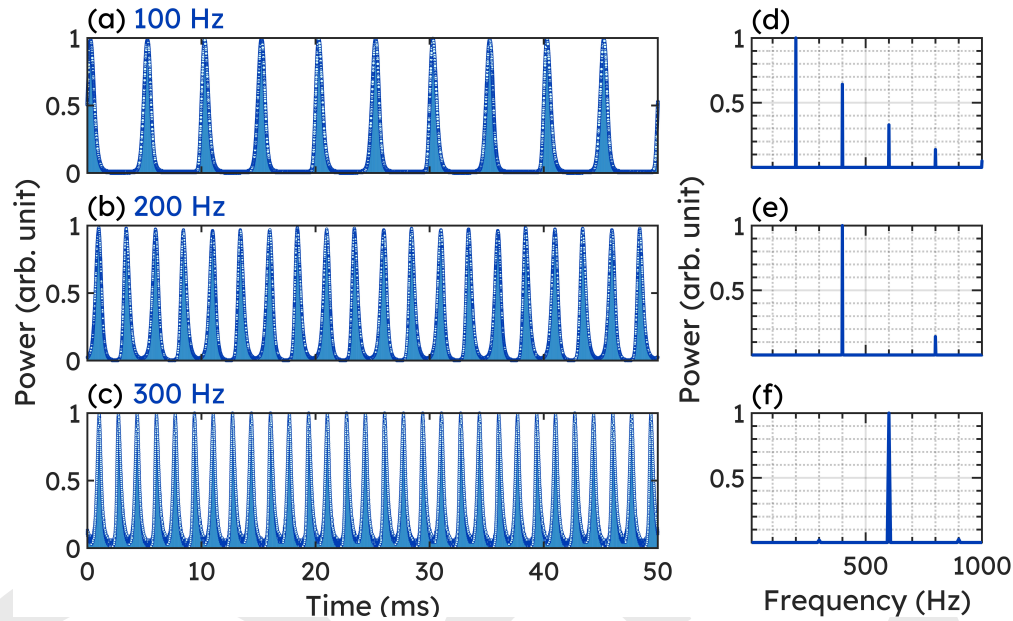
Fig. 5. Light intensity variation for scanning frequencies of (a) 100 Hz, (b) 200 Hz, and (c) 300 Hz. The scanning is performed at bias voltage of 72 V. The modulating voltage is 6 V in (a) and (b) and 12 V in (c). The fiber core is positioned at the center of the scan cycle (at 0° - on the optical axis, the scan starts from -3° to 3° and back to -3° to complete one cycle) hence, in every scanning cycle, two intensity peaks will be recorded on the photodetector. (d)–(f) Fourier transform of the time series presented in (a)–(c). The fundamental frequency evaluated through Fourier transform is double the scanning frequency as a result of the scanning method. Lastly, the periodicity of the photodetector signal results in other harmonic peaks that appear as subsequent intensity peaks in the Fourier transform.

Figure 5(a)–5(c) depicts the photodiode intensity variation for sweeping frequencies of 100, 200, and 300 Hz over a period of 50 ms. The fiber core is positioned at the center of the scan cycle (at 0° - on the optical axis, the scan starts from -3° to 3° and back to -3° to complete one cycle) hence, in every scanning cycle, two intensity peaks will be recorded on the photodetector. Intensity measurements from the photodetector were analyzed using Fourier analysis as illustrated in Fig. 5(d)–5(f). The fundamental frequency evaluated through Fourier transform is doubled from the applied scanning frequency as a result of the scanning method implemented here. Due to the periodicity of the photodetector signal, other harmonics appeared as subsequent intensity peaks in the Fourier transform. The scanning is performed at bias voltage of 72 V with modulating voltage of 6 V for 100 and 200 Hz sweeping frequencies [Fig. 5(a)–5(b)], and 12 V for 300 Hz sweeping frequency [Fig. 5(c)], respectively. The scanning angles decrease by increasing the sweeping frequencies at a given differential voltages. Increasing the differential voltage between the two electrodes compensates for the scanning angle reduction [41].

The optical switch presented here is capable of hundreds of Hz scanning frequency, has ~1 dB of insertion loss, a high extinction ratio of 47 dB, and can perform over a wide range of wavelengths. The PCH has an optical transmission of > 90% in the wavelength range of 500–1100 nm, while DI-water has a transmission of > 90% for 400–700 nm range. The extinction ratio of the demonstrated optical switch is mainly limited by the secondary rays created through glass substrates, the coupling lens, and the sidewalls of the EWOD prism.

5. Conclusion

We demonstrated a novel switching concept based on an EWOD prism coupled into a multimode fiber. The EWOD prism is filled with DI-water and PCH liquids, enabling optical switching with extinction ratio of 47 dB between the ON (high transmission) and OFF state (no transmission). The ultrasmooth, sub-nanometer surface roughness at the liquid-liquid interface enables us to perform switching with a large extinction ratio and low insertion loss. The liquid-liquid interface of the EWOD prism is modeled in Zemax to perform non-sequential ray tracing with secondary rays. The simulation predicts an extinction ratio of 50 dB between the ON and OFF state, while experimentally, we measured an extinction ratio of 47 dB. The discrepancy between the optical model and measured results are due to lack of scattering in the simulation model. We have explored the dynamic scanning speed of the EWOD prism in the proposed optical switch and find that scanning frequencies of up to 300 Hz are feasible in our design. Reducing the size of the EWOD prism can significantly enhance the scanning speed of these devices further as the response time is proportional to device radius, $\tau \sim r^{3/2}$ [12]. Lastly, a fiber coupled optical switch based on an EWOD prism is appealing for many applications due to the transmissive nature of the EWOD prism, independence from polarization, high extinction ratio, and low insertion loss.

References

1. D. R. Scherer, R. Lutwak, M. Mescher, R. Stoner, B. Timmons, F. Rogomentich, G. Tepolt, S. Mahnkopf, J. Noble, S. Chang, and D. Taylor, "Progress on a miniature cold-atom frequency standard," arXiv **1411.5006** (2014).
2. T. Guo, K. Deng, X. Chen, and Z. Wang, "Atomic clock based on transient coherent population trapping," Applied Physics Letters **94**, 151108 (2009).
3. G. Vallone, D. Bacco, D. Dequal, S. Gaiarin, V. Luceri, G. Bianco, and P. Villoresi, "Experimental satellite quantum communications," Phys. Rev. Lett. **115**, 040502 (2015).
4. Shi-Sheng Lee, Long-Sun Huang, Chang-Jin Kim, and M. C. Wu, "Free-space fiber-optic switches based on mems vertical torsion mirrors," Journal of Lightwave Technology **17**, 7–13 (1999).
5. Meng-Hsiung Kiang, O. Solgaard, K. Y. Lau, and R. S. Muller, "Electrostatic combdrive-actuated micromirrors for laser-beam scanning and positioning," Journal of Microelectromechanical Systems **7**, 27–37 (1998).
6. C. S. Adams, "A mechanical shutter for light using piezoelectric actuators," Review of Scientific Instruments **71**, 59 (2000).
7. W. Bowden, I. R. Hill, P. E. G. Baird, and P. Gill, "Note: A high-performance, low-cost laser shutter using a piezoelectric cantilever actuator," Review of Scientific Instruments **88**, 016102 (2017).
8. A. Acharya, S. De, P. Arora, and A. S. Gupta, "A universal driver for vibration free operation of mechanical shutters," Measurement **61**, 16–20 (2015).
9. W. J. Schwenger and J. M. Higbie, "High-speed acousto-optic shutter with no optical frequency shift," Review of Scientific Instruments **83**, 083110 (2012).
10. Xiaohua Ma and Geng-Sheng Kuo, "Optical switching technology comparison: optical mems vs. other technologies," IEEE Communications Magazine **41**, S16–S23 (2003).
11. Y. . Peter, F. Gonte, H. P. Herzig, and R. Dandliker, "Micro-optical fiber switch for a large number of interconnects using a deformable mirror," IEEE Photonics Technology Letters **14**, 301–303 (2002).
12. S. Kuiper and B. H. W. Hendriks, "Variable-focus liquid lens for miniature cameras," Applied Physics Letters **85**, 1128–1130 (2004).
13. C. U. Murade, D. van der Ende, and F. Mugele, "High speed adaptive liquid microlens array," Opt. Express **20**, 18180–18187 (2012).

14. R. D. Niederriter, A. M. Watson, R. N. Zahreddine, C. J. Cogswell, R. H. Cormack, V. M. Bright, and J. T. Gopinath, "Electrowetting lenses for compensating phase and curvature distortion in arrayed laser systems," Appl. Opt. **52**, 3172–3177 (2013).

15. S. A. Reza and N. A.Riza, "A liquid lens-based broadband variable fiber optical attenuator," Optics Communications **282**, 1298–1303 (2009).

16. N. R. Smith, D. C. Abeysinghe, J. W. Haus, and J. Heikenfeld, "Agile wide-angle beam steering with electrowetting microprisms," Opt. Express **14**, 6557–6563 (2006).

17. S. Terrab, A. M. Watson, C. Roath, J. T. Gopinath, and V. M. Bright, "Adaptive electrowetting lens-prism element," Opt. Express **23**, 25838–25845 (2015).

18. D. Kopp, L. Lehmann, and H. Zappe, "Optofluidic laser scanner based on a rotating liquid prism," Appl. Opt. **55**, 2136–2142 (2016).

19. L. Hou, J. Zhang, N. Smith, J. Yang, and J. Heikenfeld, "A full description of a scalable microfabrication process for arrayed electrowetting microprisms," Journal of Micromechanics and Microengineering **20**, 015044 (2009).

20. E. P. Raynes and I. A. Shanks, "Fast-switching twisted nematic electro-optical shutter and colour filter," Electronics Letters **10**, 114–115 (1974).

21. M. Ide, A. Suguro, Y. Hosaka, A. Katsunuma, K. Takahashi, and A. Shiraishi, "A pixelized variable optical attenuator using liquid crystal on silicon technology for tunable filters," Optical Review **11**, 132–139 (2004).

22. D.-Y. Zhang, V. Lien, Y. Berdichevsky, J. Choi, and Y.-H. Lo, "Fluidic adaptive lens with high focal length tunability," Applied Physics Letters **82**, 3171–3172 (2003).

23. L. Zhu, Y. Huang, and A. Yariv, "Integrated microfluidic variable optical attenuator," Opt. Express **13**, 9916–9921 (2005).

24. U. Levy and R. Shamai, "Tunable optofluidic devices," Microfluidics and Nanofluidics **4**, 97–105 (2008).

25. L. Pang, H. M. Chen, L. M. Freeman, and Y. Fainman, "Optofluidic devices and applications in photonics, sensing and imaging," Lab Chip **12**, 3543–3551 (2012).

26. S. Xu, H. Ren, and S.-T. Wu, "Dielectrophoretically tunable optofluidic devices," Journal of Physics D: Applied Physics **46**, 483001 (2013).

27. S. Schuhladen, K. Banerjee, M. Stürmer, P. Müller, U. Wallrabe, and H. Zappe, "Variable optofluidic slit aperture," Light: Science & Applications p. e16005 (2016).

28. M. Vallet, B. Berge, and L. Vovelle, "Electrowetting of water and aqueous solutions on poly(ethylene terephthalate) insulating films," Polymer **37**, 2465–2470 (1996).

29. B. Berge and J. Peseux, "Variable focal lens controlled by an external voltage: An application of electrowetting," Eur. Phys. J. E **3**, 159–163 (2000).

30. F. Mugele and J. Baret, "Electrowetting: from basics to applications," J. Phys. Condens. Matter **17**, R705–R774 (2005).

31. W. C. Nelson and C. J. Kim, "Droplet actuation by electrowetting-on-dielectric (ewod): A review," J. Adhes. Sci. Technol. **26**, 1747–1771 (2012).

32. K. Mishra, D. van den Ende, and F. Mugele, "Recent developments in optofluidic lens technology," Micromachines **7**, 102 (2016).

33. F. Mugele and J. Heikenfeld, *Electrowetting: Fundamental Principles and Practical Applications* (John Wiley & Sons, 2018).

34. H. J. J. Verheijen and M. W. J. Prins, "Reversible electrowetting and trapping of charge: Model and experiments," Langmuir **15**, 6616–6620 (1999).

35. T. Krupenkin, S. Yang, and P. Mach, "Tunable liquid microlens," Applied Physics Letters **82**, 316–318 (2003).

36. M. Kim, D. Kang, T. Wu, N. Tabatabaei, R. W. Carruth, R. V. Martinez, G. M. Whitesides, Y. Nakajima, and G. J. Tearney, "Miniature objective lens with variable focus for confocal endomicroscopy," Biomed. Opt. Express **5**, 4350–4361 (2014).

37. N. Binh-Khiem, K. Matsumoto, and I. Shimoyama, "Polymer thin film deposited on liquid for varifocal encapsulated liquid lenses," Applied Physics Letters **93**, 124101 (2008).

38. C. Li and H. Jiang, "Electrowetting-driven variable-focus microlens on flexible surfaces," Applied Physics Letters **100**, 231105 (2012).

39. A. Shahini, J. Xia, Z. Zhou, Y. Zhao, and M. M.-C. Cheng, "Versatile miniature tunable liquid lenses using transparent graphene electrodes," Langmuir **32**, 1658–1665 (2016).

40. F. Krogmann, W. Monch, and H. Zappe, "Electrowetting for tunable microoptics," Journal of Microelectromechanical Systems **17**, 1501–1512 (2008).

41. W. Y. Lim, O. Supekar, M. Zohrabi, J. Gopinath, and V. Bright, "A liquid combination with high refractive index contrast and fast scanning speeds for electrowetting adaptive optics," Langmuir **34**, 14511–14518 (2018).

42. M. S. Ober, D. Dermody, M. Daniel, M. Maillard, F. Amiot, G. Malet, B. Burger, C. Woelfle-Gupta, and B. Berge, "Development of biphasic formulations for use in electrowetting-based liquid lenses with a high refractive index difference," ACS Combinatorial Science **20**, 554–566 (2018).

43. J. Zhang, D. Van Meter, L. Hou, N. Smith, J. Yang, A. Stalcup, R. Laughlin, and J. Heikenfeld, "Preparation and analysis of 1-chloronaphthalene for highly refractive electrowetting optics," Langmuir **25**, 10413–10416 (2009).

44. D. Chatterjee, B. Hetayothin, A. R. Wheeler, D. J. M. King, and R. L. Garrell, "Droplet-based microfluidics with nonaqueous solvents and solutions." Lab on a chip **6 2**, 199–206 (2006).

45. S. Chevalliot, J. Heikenfeld, L. Clapp, A. Milarcik, and S. Vilner, "Analysis of nonaqueous electrowetting fluids for displays," J. Display Technol. **7**, 649–656 (2011).

46. D. Kopp and H. Zappe, "Tubular astigmatism-tunable fluidic lens," Opt. Lett. **41**, 2735–2738 (2016).

47. R. A. Hayes and B. J. Feenstra, "Video-speed electronic paper based on electrowetting," Nature **425**, 383–385 (2003).

48. K. Zhou, J. Heikenfeld, K. A. Dean, E. M. Howard, and M. R. Johnson, "A full description of a simple and scalable fabrication process for electrowetting displays," Journal of Micromechanics and Microengineering **19**, 065029 (2009).

49. H. You and A. J. Steckl, "Three-color electrowetting display device for electronic paper," Applied Physics Letters **97**, 023514 (2010).

50. G. Yang, B. Tang, D. Yuan, A. Henzen, and G. Zhou, "Scalable fabrication and testing processes for three-layer multi-color segmented electrowetting display," Micromachines **10** (2019).

51. P. Müller, A. Kloss, P. Liebetraut, W. Mönch, and H. Zappe, "A fully integrated optofluidic attenuator," Journal of Micromechanics and Microengineering **21**, 125027 (2011).

52. P. Müller, R. Feuerstein, and H. Zappe, "Integrated optofluidic iris," Journal of Microelectromechanical Systems **21**, 1156–1164 (2012).

53. L. Li, C. Liu, H. Ren, and Q.-H. Wang, "Adaptive liquid iris based on electrowetting," Opt. Lett. **38**, 2336–2338 (2013).

54. C.-C. Yu, J.-R. Ho, and J. W. J. Cheng, "Tunable liquid iris actuated using electrowetting effect," Optical Engineering **53**, 1–5–5 (2014).

55. H. W. Seo, J. B. Chae, S. J. Hong, K. Rhee, J. hyeon Chang, and S. K. Chung, "Electromagnetically driven liquid iris," Sensors and Actuators A: Physical **231**, 52–58 (2015).

56. J. Heikenfeld and A. J. Steckl, "High-transmission electrowetting light valves," Applied Physics Letters **86**, 151121 (2005).

57. C. Liu, L. Li, and Q.-H. Wang, "Bidirectional optical switch based on electrowetting," Journal of Applied Physics **113**, 193106 (2013).

58. P. Müller, D. Kopp, A. Llobera, and H. Zappe, "Optofluidic router based on tunable liquid–liquid mirrors," Lab Chip **14**, 737–743 (2014).

59. C. Liu, D. Wang, L.-X. Yao, L. Li, and Q.-H. Wang, "Electrowetting-actuated optical switch based on total internal reflection," Appl. Opt. **54**, 2672–2676 (2015).

60. R. D. Montoya, K. Underwood, S. Terrab, A. M. Watson, V. M. Bright, and J. T. Gopinath, "Large extinction ratio optical electrowetting shutter," Opt. Express **24**, 9660–9666 (2016).

61. F. Ribet, E. De Luca, F. Ottonello-Briano, M. Swillo, N. Roxhed, and G. Stemme, "Zero-insertion-loss optical shutter based on electrowetting-on-dielectric actuation of opaque ionic liquid microdroplets," Applied Physics Letters **115**, 073502 (2019).

62. J. Lee, Y. Park, and S. K. Chung, "Switchable liquid shutter for security and design of mobile electronic devices," in "2018 IEEE Micro Electro Mechanical Systems (MEMS)," (2018), pp. 14–16.

63. C. Liu, D. Wang, and Q.-H. Wang, "Variable aperture with graded attenuation combined with adjustable focal length lens," Opt. Express **27**, 14075–14084 (2019).

64. X. Wang and H. Ren, "Dielectrically actuated attenuator at 1.55 μm," Journal of Physics Communications **2**, 085026 (2018).

65. M. L. Schlossman, "Liquid-liquid interfaces: studied by x-ray and neutron scattering," Current Opinion in Colloid & Interface Science **7**, 235–243 (2002).

66. M. K. Sanyal, S. K. Sinha, K. G. Huang, and B. M. Ocko, "X-ray-scattering study of capillary-wave fluctuations at a liquid surface," Phys. Rev. Lett. **66**, 628–631 (1991).

67. G. Luo, S. Malkova, S. V. Pingali, D. G. Schultz, B. Lin, M. Meron, T. J. Graber, J. Gebhardt, P. Vanysek, and M. L. Schlossman, "X-ray studies of the interface between two polar liquids: neat and with electrolytes," Faraday Discuss. **129**, 23–34 (2005).

68. J. B. Chae, J. O. Kwon, J. S. Yang, D. Kim, K. Rhee, and S. K. Chung, "Optimum thickness of hydrophobic layer for operating voltage reduction in ewod systems," Sensors and Actuators A: Physical **215**, 8–16 (2014).

69. K. L. Mittal, *Advances in Contact Angle, Wettability and Adhesion, Volume 1* (ohn Wiley & Sons, 2013).

70. K. L. Mittal, *Advances in Contact Angle, Wettability and Adhesion, Volume 2* (ohn Wiley & Sons, 2015).

71. K. L. Mittal, *Advances in Contact Angle, Wettability and Adhesion, Volume 3* (John Wiley & Sons, 2018).

72. L. Li, D. Wang, C. Liu, and Q.-H. Wang, "Zoom microscope objective using electrowetting lenses," Opt. Express **24**, 2931–2940 (2016).

73. B. N. Ozbay, J. T. Losacco, R. Cormack, R. Weir, V. M. Bright, J. T. Gopinath, D. Restrepo, and E. A. Gibson, "Miniaturized fiber-coupled confocal fluorescence microscope with an electrowetting variable focus lens using no moving parts," Optics Letter **40**, 2553–2556 (2015).

74. B. N. Ozbay, G. L. Futia, M. Ma, V. M. Bright, J. T. Gopinath, E. G. Hughes, D. Restrepo, and E. A. Gibson, "Three dimensional two-photon brain imaging in freely moving mice using a miniature fiber coupled microscope with active axial-scanning," Scientific Reports **8** (2018).

75. K. F. Tehrani, C. V. Latchoumane, W. M. Southern, E. G. Pendleton, A. Maslesa, L. Karumbaiah, J. A. Call, and L. J. Mortensen, "Five-dimensional two-photon volumetric microscopy of in-vivo dynamic activities using liquid lens remote focusing," Biomed. Opt. Express **10**, 3591–3604 (2019).

76. O. D. Supekar, B. N. Ozbay, M. Zohrabi, P. D. Nystrom, G. L. Futia, D. Restrepo, E. A. Gibson, J. T. Gopinath, and

V. M. Bright, "Two-photon laser scanning microscopy with electrowetting-based prism scanning," Biomed. Opt. Express **8**, 5412–5426 (2017).

77. M. Zohrabi, W. Y. Lim, R. H. Cormack, O. D. Supekar, V. M. Bright, and J. T. Gopinath, "Lidar system with nonmechanical electrowetting-based wide-angle beam steering," Opt. Express **27**, 4404–4415 (2019).

78. M. Zohrabi, R. H. Cormack, C. Mccullough, O. D. Supekar, E. A. Gibson, V. M. Bright, and J. T. Gopinath, "Numerical analysis of wavefront aberration correction using multielectrode electrowetting-based devices," Opt. Express **25**, 31451–31461 (2017).

79. N. C. Lima, A. Cavalli, K. Mishra, and F. Mugele, "Numerical simulation of astigmatic liquid lenses tuned by a stripe electrode," Opt. Express **24**, 4210–4220 (2016).

80. Y.-Y. Lin, R. D. Evans, E. Welch, B.-N. Hsu, A. C. Madison, and R. B. Fair, "Low voltage electrowetting-on-dielectric platform using multi-layer insulators," Sensors and Actuators B: Chemical **150**, 465–470 (2010).

81. M. Mibus and G. Zangari, "Performance and reliability of electrowetting-on-dielectric (ewod) systems based on tantalum oxide," ACS Applied Materials & Interfaces **9**, 42278–42286 (2017).

82. A. Schultz, S. Chevalliot, S. Kuiper, and J. Heikenfeld, "Detailed analysis of defect reduction in electrowetting dielectrics through a two-layer 'barrier' approach," Thin Solid Films **534**, 348–355 (2013).

83. L. Huang, B. Koo, and C. Kim, "Sputtered-anodized Ta_2O_5 as the dielectric layer for electrowetting-on-dielectric," Journal of Microelectromechanical Systems **22**, 253–255 (2013).

84. OpticStudio Zemax, User's Manual, v. 19, https://www.zemax.com/products/opticstudio/ (2019).

85. R. Finn, *Equilibrium capillary surfaces* (Springer-Verlag, 1986).

86. C. F. Scott, G. C. Sander, and J. Norbury, "Computation of capillary surfaces for the laplace-young equation," The Quarterly Journal of Mechanics and Applied Mathematics **58**, 201–212 (2005).

87. S.-L. Lee and H.-D. Lee, "Evolution of liquid meniscus shape in a capillary tube," ASME J. Fluids Eng. **129**, 957–965 (2007).

88. S.-L. Lee and C.-F. Yang, "Numerical simulation for meniscus shape and optical performance of a mems-based liquid micro-lens," Opt. Express **16**, 19995–20007 (2008).

89. J. C. Berg, *An Introduction to Interfaces and Colloids* (World Scientific, 2009).

90. M. A. Rodríguez-Valverde, M. A. Cabrerizo-Vílchez, and R. Hidalgo-Álvarez, "The young laplace equation links capillarity with geometrical optics," European Journal of Physics **24**, 159–168 (2003).

91. COMSOL Multiphysics Reference Manual, v. 5.1, http://www.comsol.com/ (2018).

92. T. Satyanarayana, G. A. K. Reddy, and V. S. P. Rajesh, "Design and simulation of micro electro wetting liquid lens for miniature cameras," in "International Journal of Science and Research (IJSR)," , vol. 2 (2013), vol. 2.

93. W. M. Salman, H. A. Ali, M. S. Abdelsalam, M. F. F. El-Dosoky, and M. Abdelgawad, "Interfacial electrical shear stresses induce electrohydrodynamic flows inside droplets actuated by electrowetting," in "ASME International Mechanical Engineering Congress and Exposition," , vol. 7B (2015), vol. 7B.

94. O. D. Supekar, M. Zohrabi, J. T. Gopinath, and V. M. Bright, "Enhanced response time of electrowetting lenses with shaped input voltage functions," Langmuir **33**, 4863–4869 (2017). PMID: 28431469.

95. S. Wang, J. Shi, H.-H. Chen, T. Xu, and C.-L. C. L. Chen, "Numerical and experimental investigation of bubble dynamics via electrowetting-on-dielectric (ewod)," in "International Conference on Micro/Nanoscale Heat Transfer," , vol. 1 (2016), vol. 1.